Identifying efficient transport pathways in early-wood timber

Insights from 3D X-ray CT imaging of softwood in the presence of flow

**H. C. Burridge · R. Pini* · S. M. K.
Shah · T. P. S. Reynolds · G. Wu · D.
U. Shah · O. A. Scherman · M. H.
Ramage · P. F. Linden**

Abstract Wider use of timber has the potential to greatly reduce the embodied carbon of construction. Improved chemical treatment could help overcome some of the barriers to wider application of timber, by furthering the durability and/or mechanical properties of this natural material. Improving timber treat-

H. C. Burridge
Department of Civil and Environmental Engineering, Imperial College London, London SW7 2AZ, UK

R. Pini
Department of Chemical Engineering, Imperial College London, London SW7 2AZ, UK
Tel.: +44 (0)20 7594 7518
E-mail: r.pini@imperial.ac.uk

S. M. K. Shah
Department of Chemical Engineering, Imperial College London, London SW7 2AZ, UK
Present address: UCL Mechanical Engineering, Research Complex at Harwell, RAL, Didcot, Oxfordshire, OX11 0FA, UK

T. P. S. Reynolds
Institute for Infrastructure and Environment, School of Engineering, University of Edinburgh, Edinburgh EH9 3FG, UK

G. Wu
Melville Laboratory for Polymer Synthesis, Department of Chemistry, University of Cambridge, Lensfield Road, Cambridge CB2 1EW, UK

D. U. Shah
Department of Architecture, University of Cambridge, Cambridge CB2 1PX, UK

O. A. Scherman
Melville Laboratory for Polymer Synthesis, Department of Chemistry, University of Cambridge, Lensfield Road, Cambridge CB2 1EW, UK

M. H. Ramage
Department of Architecture, University of Cambridge, Cambridge CB2 1PX, UK

P. F. Linden
Department of Applied Mathematics and Theoretical Physics, University of Cambridge, Centre for Mathematical Sciences, Wilberforce Road, Cambridge CB3 0WA, UK

ment by treating the whole volume of a piece of timber, or tailored sections thereof, requires sound understanding and validated modelling of the natural paths for fluid flow through wood. In this study we carry out a robust analysis of three-dimensional X-ray CT measurements on kiln-dried softwood in the presence of flow and identify small portions of early-wood which are uniquely capable of transporting fluids — herein 'efficient transport pathways'. We successfully model the effects of these pathways on the liquid uptake by timber by introducing a spatial variability in the amount of aspiration of the bordered pits following kiln drying. The model demonstrates that fluid advances along these efficient transport paths between 10 and 30 times faster than in the remainder of the timber. Identifying these efficient transport pathways offers scope to improve and extend the degree to which timber properties are enhanced at an industrial scale through processes to impregnate timber.

1 Introduction

Wood provides both structural support for the tree and acts as a conduit for flow; both properties derive from the timber micro-structure. A significant body of work relates the timber micro-structure to its mechanical properties [1,2] whilst, until recently, little work has related observations of the micro-structure to its transport properties [3]. The understanding of wood's transport properties are of relevance to the treatment of wood to improve its mechanical properties and/or durability [4–6], the preservation of archaeological timbers [7], and understanding the process of water transport in living trees.

Radiographic examination of softwood timber specimens, motivated by its impregnation for preservative treatment, is not new [8–10], but remains highly relevant. However, unlike in industrial processes, all studies thus far have relied on spontaneous imbibition and capillary action to drive the flow — herein, we force the flow by imposing moderate pressure gradients of $\sim 1.5\,\mathrm{MPa/m}$ across the specimens. More recent radiographic studies of timber include [11] who make quantitative measurements of the liquid uptake in small ($\sim 1\,\mathrm{ml}$) softwood specimens. They conclude that transport occurred mainly through the lumen and the predominant restriction to flow was the bordered pits. They observed non-uniform transport and report preferential transport in the smaller late-wood cells, surmising that higher capillary forces led to the preferential transport. Similar observations were made by [12] and [13].

Recently [3], we measured liquid uptake by forcing chloroform (with imposed pressures of 0.1 and 0.15 MPa) to intrude softwood specimens of length 70 mm, showing that the uptake exhibited a significant departure from a classical square-root-of-time behaviour (as has been previously observed [14,15, 11]). Moreover, this departure was successfully modelled by using a modification of the Lucas-Washburn equation [16,17], which accounts for the statistical variation in the timber pore space. The model was parameterised such that

smaller late-wood cells exhibited the least resistance to flow and hence constituted the preferential pathways for flow. However, it was shown that even at these modest imposed pressure gradients ($\sim 1.4 - 2.1\,\mathrm{MPa/m}$), capillary forces only accounted for a fraction ($\sim 10\%$) of the liquid transport, with the remainder of the transport driven by the imposed pressure gradients.

In the present work, we resolve this apparent inconsistency by showing that the preferential transport did occur in the late-wood when only capillary forces drive the flow. Furthermore, we show that there are cells, some of the first early-wood cells laid down by the tree each year, which are uniquely able to transport liquids more efficiently. It is these cells that, in the presence of moderate imposed pressure gradients, dominate the flow. We argue that the reason for this is the greater tendency of the first early-wood pits to resist aspiration caused by kiln drying. We validate this hypothesis by using a model that accounts for this spatial variability in the degree of pits aspiration.

2 Experimental

We conducted two experiments on a specimen of Sitka spruce (*Picea sitchensis* (Bong.) Carrière), as reported in Table 1 together with the conditions of the tests. Two spontaneous imbibition tests were also carried out on a separate sample of the same species and these are described in Section 2.4.

Exp No.	Fluid	P_c	P_{inj}	V_{inj}	t_{inj}	ρ_b	ϕ
		MPa	MPa	mL	min	g/mL	%
1	W	0.8	0.4	108	1374	0.379	72.4
2	EA	0.8	0.4	475	388	0.380	72.4

Table 1 List of experiments carried out in this study. These have been conducted by injecting liquid (water, W, or ethyl acetate, EA) at constant pressure (P_{inj}). During each experiment, the specimen was kept under a constant external pressure (P_c) and the volume of injected liquid (V_{inj}) was continuously recorded by the pump. The specimen bulk density (ρ_b) is estimated from mass/geometrical volume and its porosity is obtained by assuming an average specimen skeletal density of $\rho_s = 1.37$ g/cm^3.

2.1 Materials

A 200 mm-long specimen was machined into a cylindrical shape (50 mm in diameter) from flat-sawn, kiln-dried timber supplied by BSW Timber Ltd (UK). From a first visual inspection (see also Figure 1), the specimen accommodates six growth rings, which are approximately parallel to one another (~ 1 cm apart) and aligned with the longitudinal axis, z, which also corresponds to the direction of flow imposed in the experiments. These growth rings cover the full length of the specimen, but are distorted by the presence of a knot which

crosses the entire specimen at a slight angle to the vertical direction, y. The specimen bulk density, estimated from mass/geometrical volume, takes a value $\rho_{\mathrm{b}} = 0.38\,\mathrm{g/cm^3}$. An average specimen porosity of $\phi = 72.5\%$ is obtained by assuming an average specimen skeletal density of $\rho_{\mathrm{s}} = 1.37\,\mathrm{g/cm^3}$. The latter has been obtained by [18] from Helium pycnometry on consolidated sister specimens and is lower than the so-called dry cell wall density ($\rho_{\mathrm{m}} \approx 1.5\,\mathrm{g/cm^3}$) due to the presence of inaccessible pores and/or closed lumens (see [18] for a full discussion). Two liquids were used for the solvent injection experiments, namely de-ionized water and ethyl acetate (anhydrous, 99.8%, Sigma Aldrich), as these solvents produce a different degree of tangential swelling of Sitka spruce, namely 8.4% (water) and 2.6% (ethyl acetate), respectively [19]. The relevant physical properties of the two liquids are provided in Table 2.
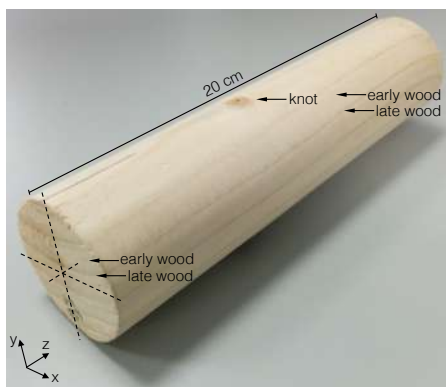

Fig. 1 Photograph of the Sitka spruce specimen used in this study. The radial and tangential planes of the timber correspond to the $x - y$ and $x - z$ planes, respectively. During the experiments, solvent injection takes place along the longitudinal axis of the specimen (z).

Property	Water	Ethyl Acetate
Density, ρ_{l} [g/cm^3]	0.997	0.894
Viscosity, μ_{l} [cP]	0.890	0.418
Surface tension,γ [mN/m]	71.6	23.4
Relative polarity [-]	1.000	0.228

Table 2 Physical properties of the solvents used in this study. Density, viscosity and surface tension have been extracted from the Springer Materials database (http://materials.springer.com), while values for the relative polarity are obtained from Reichardt C., Solvents and Solvent Effects in Organic Chemistry, Wiley-VCH Publishers, 3rd ed., 2003.

2.2 Apparatus

The solvent injection experiments were performed using the experimental setup depicted in Figure 2. A custom-made aluminum specimen-holder has been used that can accommodate a cylindrical specimen of 5 cm in diameter and of variable length. The specimen is positioned between two aluminum end-plates with embedded circular grooves for enhanced fluid distribution (see inset in the figure). Due to timber's fairly large permeability, two layers of qualitative filter paper (Whatman, Grade 1, 11 μm pore size) are additionally placed between the inlet face of the specimen and the aluminum end-plate, so as to minimise boundary effects caused by the detail of the end-cap. The whole arrangement is jacketed with two layers of polyolefin heat shrink tubing (RS Pro, UK) to achieve a tight seal around the specimen. To further minimise bypass flow during the experiments, the annulus between the jacketed specimen and the aluminum specimen-holder is filled with water that is kept at a constant pressure P_c using a syringe pump (ISCO Teledyne, Model 1000D). The specimen-holder is placed horizontally on the bed of the scanning instrument (Universal Systems HD-350 X-ray CT scanner) and is connected to an injection pump (ISCO Teledyne, Model 1000D) and an effluent collector by means of 1/16" OD PEEK tubing. Two high-accuracy pressure transducers (Keller UK, Model PA-33X) are connected through tubing ported directly to the inlet and outlet faces of the core. These are continuously logged throughout the experiment by a Data Acquisition PC (DAQ PC), together with flow rates, pressures and cumulative volumes recorded by the pumps.
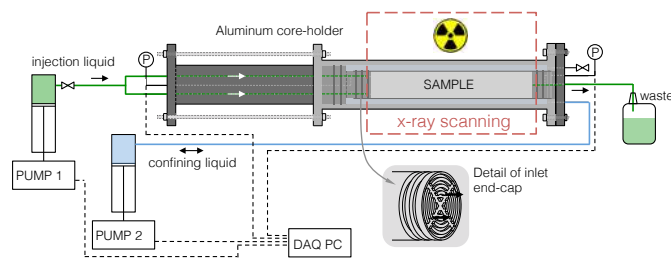
Fig. 2 Simplified schematic (not to scale) of the apparatus used for solvent injection studies in timber with simultaneous imaging by X-ray Computed Tomography (CT).

2.3 Experimental procedure and X-ray imaging

Water and ethyl acetate were used as injection fluids (in this chronological order) and both experiments have been carried out at room temperature and ambient pressure conditions. Prior to each experiment, the timber specimen was dried for 24 hours at 60°C and subsequently stored in the laboratory in air (r.H. $\approx$ 30%). The similarity of the dry 3D density profiles obtained prior

to the experiment with water and ethyl acetate (see Results section) indicates that the microstructure of the specimen has not been altered by the drying process. After assembling the aluminum specimen-holder and placing it on the bed of the scanner, the annular confining pressure on the specimen was increased and set to a value of 0.8 MPa. A full X-ray scan was taken of the dry specimen, which was subsequently no longer moved. The injection lines were then purged with the solvent, connected to the inlet end-cap and injection started. For the experiments reported here, the latter was achieved by maintaining a constant injection pressure of 0.4 MPa, while keeping the effluent line open to atmospheric pressure (i.e. a pressure drop, $\Delta P = 0.3$ MPa). Stable injection pressure was achieved within 1 minute. Throughout the experiment, X-ray scans of the specimen were taken at regular time intervals for 2-mm-thick slices at a resolution of $(250 \times 250)\,\mu\mathrm{m}^2$ and an acquisition time of approximately 10 min for one full tomogram. Additional imaging parameters are: field-of-view, 120 mm; energy level of radiation, 120 eV; tube current, 200 mA).

The X-ray tomograms reconstructed by the scanner are provided in terms of 2D maps of spatially distributed CT numbers in Hounsfield units, HU. For X-ray energies above 100 keV, i.e. where medical CT scanners normally operate, the CT number can safely be assumed to be linearly proportional to the bulk density of the scanned object, i.e. $\rho_\mathrm{b} = m\mathrm{CT} + p$, where m and p are constant parameters that can be obtained upon calibrating the instrument with appropriate phantoms [20]. Ideally, the latter are chosen, so as to cover the expected range of dry and wet bulk density values, thus avoiding extrapolation. This linear relationship between density and Hounsfield numbers has been previously validated for wood samples representing a large range of densities $(130 - 1300 \text{ kg} \cdot \text{m}^{-3})$ and for the current voltage applied in our study [21]. The CT number for any given voxel i in the system can be expressed as the summation of the volumetric fractions of each component in the mixture [22],

$$\overline{\mathrm{CT}}_i = (1 - \phi_i)\mathrm{CT}_\mathrm{s} + \phi_i \left[S_i \mathrm{CT}_\mathrm{l} + (1 - S_i)\mathrm{CT}_\mathrm{air} \right] \tag{1}$$

where CT_s, CT_l and CT_air are the CT numbers of the pure components (solid material, liquid and air, respectively), while ϕ and S are the porosity and the liquid saturations, which may vary from voxel to voxel. In this study, because of the fairly low density of timber ($\rho_\mathrm{b} \approx 0.4 - 1.1$ g$\cdot$cm^{-3} in the dry and fully water-wet state), air and water were used as calibration standards and the following parameters were obtained: $m = 1.04 \times 10^{-3}$ g$\cdot$cm$^{-3} \cdot$HU^{-1} and $p = 0.935$ g$\cdot$cm^{-3}. Hence, direct estimation of bulk density values from the CT numbers is possible and, accordingly, of the mass of liquid uptake per unit (bulk) volume, i.e.

$$m_\mathrm{l} = \rho_\mathrm{b,wet} - \rho_\mathrm{b,dry} = m \left(\overline{\mathrm{CT}}_\mathrm{wet} - \overline{\mathrm{CT}}_\mathrm{dry} \right) \tag{2}$$

where the subscript "dry" and "wet" refer to scans acquired prior to ($S = 0$) and after start of liquid injection. Note that (2) is applied on the voxel scale, whereas slice- (or specimen-) averaged properties are calculated using slice-

(or specimen-) averaged CT numbers. The corresponding porosity ($\phi = 1 - \rho_{b,dry}/\rho_s$) and liquid saturation values ($S = m_l/\phi\rho_l$) can be estimated by further assuming in (1) that the CT number (and, therefore, the density) of the solid component doesn't vary spatially; this assumption is justified in view of the rather uniform chemical composition of timber in terms of its three major constituents (cellulose, hemicellulose and lignin) [23].

3D reconstructions of the timber specimen are obtained using $(0.5 \times 0.5 \times 2)\,\text{mm}^3$ voxels, thereby enabling the estimation of the properties above at the voxel scale with a precision of $\rho_b \pm 4.5 \times 10^{-3}\,\text{g·cm}^{-3}$, $m_l \pm 7 \times 10^{-3}\,\text{g·cm}^{-3}$, $\phi \pm 0.35\%$ and $S \pm 1\%$. High-resolution imaging was attained for a selected slice located 100 mm from the inlet face of the specimen by acquiring (and averaging) 15 repeated scans following the acquisition of the full tomogram; this enables achieving a precision of $\pm 1 \times 10^{-3}\,\text{g·cm}^{-3}$ on the estimated density values at the original scanner resolution of $(250 \times 250)\,\mu\text{m}^2$. Images reconstruction and data analysis were carried out using in-house MATLAB routines.

2.4 Spontaneous imbibition tests

For the spontaneous imbibition experiments, a new 50 mm-long, 200 mm-diameter cylindrical specimen of Sitka spruce was used. Prior to this experiment, the specimen was dried for 24 hours at 60°C and subsequently stored in the laboratory in air (r.H. $\approx 30\%$). The specimen was wrapped in a FEP heat-shrink tube (Polyflon Technology Ltd.) and placed vertically in a plastic beaker. The heat-shrink tube was cut longer than the timber specimen, so as to leave a gap of about 5 mm between the bottom face of the wood specimen and the base of beaker. The whole arrangement was positioned on the bed of the scanning instrument. To initiate the imbibition experiment, water was carefully poured into the beaker to reach a level 15 mm above the bottom face of the timber specimen. The specimen was imaged at ambient conditions (20°C) using the X-ray CT scanner. X-ray scans of a 1 mm-thick central section of the specimen were taken prior to and during the imbibition process at regular time intervals at a resolution of $(250 \times 250)\,\mu\text{m}^2$ (additional imaging parameters: field-of-view, 120 mm; energy level of radiation, 120 eV; tube current, 200 mA). The scan analysed in this study was taken 70 hours after the start of the experiment.

An additional imbibition test was carried out on a smaller specimen to be imaged at a higher spatial resolution in a Zeiss Xradia 500 Versa 3D X-ray microscope. The small wood plug was drilled from the larger specimen to yield a 7 mm-long, 4 mm-diameter cylindrical specimen. The specimen was wrapped in a heat-shrink tube and subsequently its base attached to a specimen-holder that fits to the rotation stage of the imaging instrument using a two-component glue. The glue was applied carefully just before its hardening point to avoid its penetration into the wood specimen. To initiate the imbibition experiment, the gap (of a few mm) created by the heat-shrink on the top end of the specimen was filled with water, which was doped with

potassium iodide (25 wt%) to enhance image contrast. The specimen was imaged at ambient conditions (20°C) with 80 kV and 7 W settings prior and during imbibition (approximately 5 min after start of the experiment). The images were binned during scanning to obtain a size of 1000^3 voxels. For each tomogram, 1000 projections were taken, with a resulting computed pixel dimension of 4 μm/pixel. The tomograms were reconstructed using proprietary software provided by Zeiss. The reconstructed tomograms were processed by using Avizo-9 software.

3 Results

3.1 Three-dimensional imaging of liquid transport

X-ray CT scanning allows for precise three-dimensional imaging of the bulk density of large timber specimens at a resolution of 0.5 mm^3. Figure 3 shows a reconstruction sliced through its centre both vertically and horizontally for the dry timber specimen. The denser wood constituting the knot and the late-wood growth rings are clearly visible features in this specimen, varying in density between approximately $0.2\,\mathrm{g\cdot cm^{-3}}$ and $0.6\,\mathrm{g\cdot cm^{-3}}$.
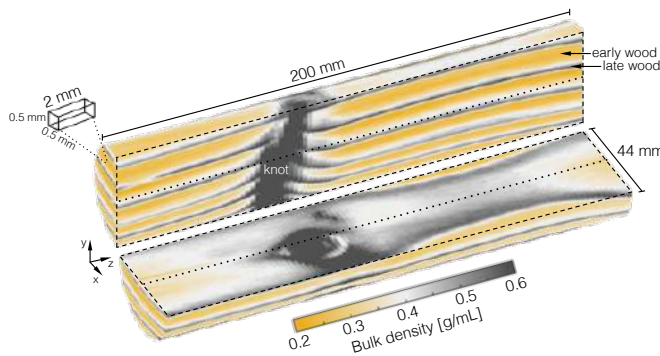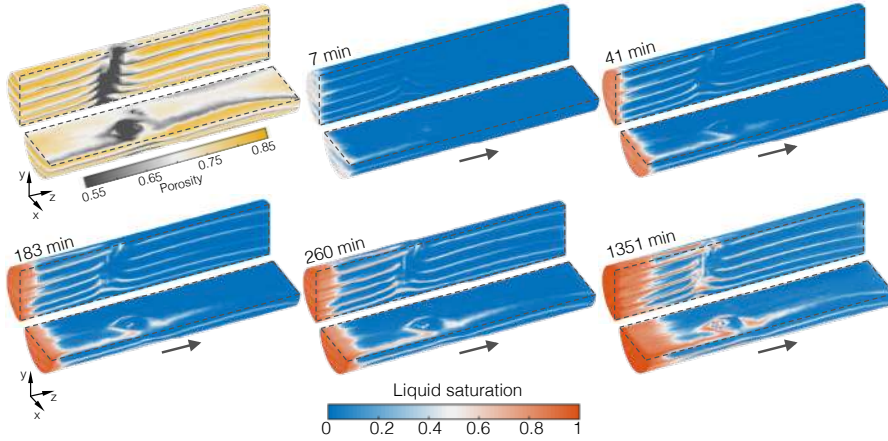

Fig. 3 3D reconstruction of the dry timber specimen in terms of bulk density, ρ_b. Voxel dimensions are $(0.5{\times}0.5{\times}2)\mathrm{mm}^3$.

X-ray CT scans of the same specimens were also obtained in the presence of liquid flow, enabling the three dimensional mapping of the liquid saturation in the timber specimen upon combination with data from the dry scan. Figure 4 shows the same timber specimen, with the top left-hand image presenting the reconstruction in terms of local (voxel) porosity. The remaining five images in the figure show these saturation maps at various time intervals throughout the experiment (in this case lasting over 22 hours) injecting water. As one would expect, the highest levels of saturation are evident at the injection end. However, we observe that in all images the locations with high levels of liquid saturation closely follow the the pattern of the late-wood growth rings. It is

evident (for example the image labeled 183 min) that water traveling along these paths reaches the far end much quicker than water being injected along other paths. Indeed it was observed that water broke through the end of the specimen at these certain locations as early as 150 minutes into the experiment.


Fig. 4 3D reconstructions of the timber specimen acquired during the water injection experiment. The map on the top left corner represents the porosity, ϕ, of the specimen (acquired prior to starting injection), while the remaining maps represent liquid saturations, S, and refer to different times throughout the experiment. Injection is carried out at a constant inlet and outlet pressures of 0.4 and 0.1 MPa, respectively. One full tomogram is acquired in about 10 min and the time shown on top of the map represents the mean between first and last scan. Voxel dimensions are $(0.5 \times 0.5 \times 2)$mm^3 and direction of flow is from left to right.

This pattern of pathways of relatively high saturation, resembling the form of the late-wood growth rings, was even more quickly evident when the specimen was injected with ethyl acetate, a solvent which causes less swelling in wood than water [19] (Figure 5). Again, the regions of high saturation also portray the outline of the knot within the specimen, highlighting that cells around the knot saturate more easily and enable relatively efficient liquid transport around and past the knot.

For a qualitative examination of the liquid uptake and saturation we selected data from the location $z = 15$ mm. A location near the inlet was chosen so that in both experiments high saturation levels could be evidenced. The left-hand images in Figure 6 show the porosity map on this 2D plane. The subsequent images show the saturation at this plane at increasing time with data from the water injections shown in the top images and that for ethyl acetate shown in the lower images. The times of the first five saturation maps are broadly similar, with the sixth (right-hand images) showing the high saturation levels reached in this plane for the (longer running) water experiment. The first five saturation maps highlight similar patterns in saturation and further show that ethyl acetate more quickly saturates the specimen, indicating faster uptake.
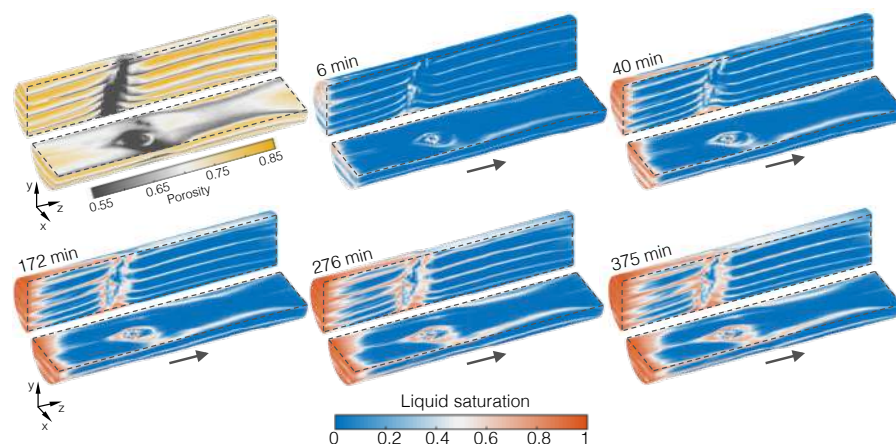
Fig. 5 3D reconstructions of the timber specimen acquired during the ethyl acetate injection experiment. The map on the top left corner represents the porosity, ϕ, of the specimen (acquired prior to starting injection), while the remaining maps represent liquid saturations, S, and refer to different times throughout the experiment. Injection is carried out at a constant inlet and outlet pressures of 0.4 and 0.1 MPa, respectively. One full tomogram is acquired in about 10 min and the time shown on top of the map represents the mean between first and last scan. Voxel dimensions are $(0.5 \times 0.5 \times 2) \text{mm}^3$ and direction of flow is from left to right.
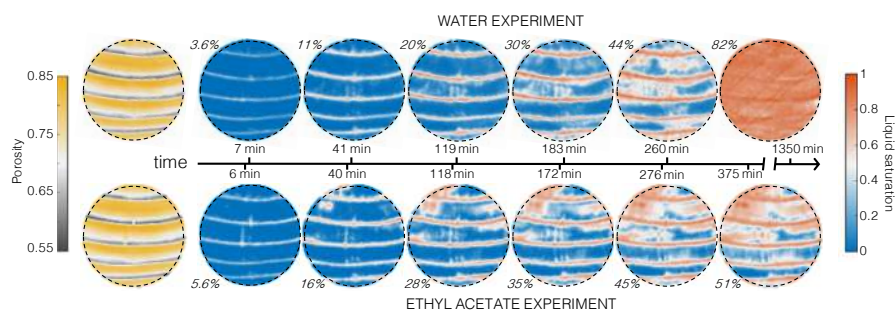

Fig. 6 2D maps of liquid saturation within one slice of the timber specimen located 15 mm from the injection port for the experiments with water (top) and ethyl acetate (bottom). Time of acquisition is shown along the central arrow, while average liquid saturation values are provided in italic. The first maps on the left represent porosity and have been acquired prior to starting each experiment. Voxel dimensions are $(500 \times 500) \mu\text{m}^2$.

3.2 Localisation of efficient transport pathways

Quantitative differences in the uptake are better evidenced by examining the central plane ($z = 100\,\text{mm}$) of the specimen. Figure 7g shows a 2D density map of the specimen at this plane taken prior to the injection of water. Examining the central transect of this plane (dashed vertical line) one can extract profiles of bulk density from the scans taken prior to (Figure 7a for water and Figure 7d for ethyl acetate) and during liquid injection (Figure 7b for water and Figure

237 7e for ethyl acetate). Profiles of liquid mass content in the specimen can be
238 readily obtained by subtracting the two sets of data (wet and dry profiles)
239 and are shown in Figure 7c (water) and Figure 7f (ethyl acetate), respectively.
240 The faster uptake of ethyl acetate is clearly evidenced by higher mass contents
241 being attained at 375 min than were attained for water at 1350 min. Within
242 the six plots of Figure 7, dashed horizontal lines mark the location of the
243 dry density peaks and aid careful observation of the relative position of the
244 peaks in liquid mass content. It can be observed that for both water and ethyl
245 acetate experiments the two sets of peaks are not precisely aligned - the peaks
246 in liquid mass content occur at locations systematically below the peaks in
247 dry bulk density. This indicates that whilst the saturation patterns in Figures
248 4, 5, and 6 mimic the pattern of the late-wood growth rings the patterns are
249 not co-located and are, in fact, offset slightly from one another. Note that
250 the liquid transport along these paths is relatively fast as the offset is already
251 apparent at early times (6-7 min after injection).
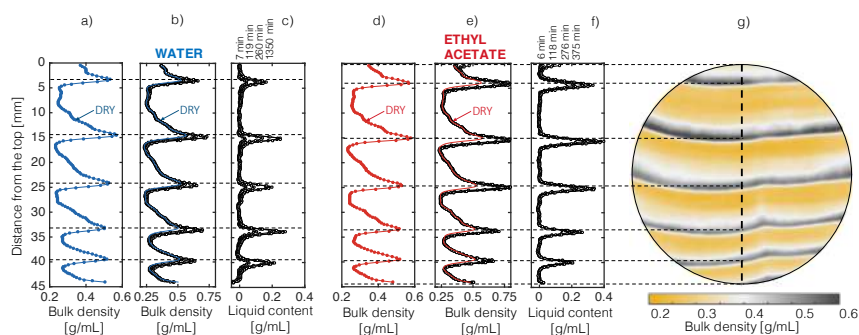
Fig. 7 2D map of bulk density (ρ_b) for one slice of the timber specimen located 100 mm from the injection port (voxel dimensions: $(250 \times 250)\mu m^2$). The corresponding 1D profiles along the vertical central transect of the slice are shown in the adjacent plots for the experiments with water (plots a-b) and ethyl acetate (plots d-e) together with those obtained in terms of liquid content (m_l) at various times after start of injection (plot c for water and plot f for ethyl acetate).

252 To better evidence this offset between peaks in density and liquid mass con-
253 tent, data was collated from ~ 100 vertical transects at the plane $z = 100$ mm
254 and the origin of a local coordinate was established at each density maximum
255 within a single transect (corresponding to a late-wood growth ring). The result-
256 ing 459 (dry) bulk density profiles in these local coordinates are plotted in the
257 lower two panes of Figure 8. The curvature of the growth rings (for example,
258 see the inset 2D density maps) highlights that the growth of the tree occurred
259 from the top to the bottom of the specimen in our particular alignment. To
260 the left of the origin (density maximum) the spatial gradient in density is more
261 gradual, whilst to the right the density drops rapidly (corresponding to the
262 tree growth ceasing over winter and then restarting, laying down much lower-
263 density wood, with the onset of the growing season). The strong similarity

between the two independent sets of dry data indicate that the drying procedure prior to each experiment didn't alter the wood's microstructure. The upper two panes show the corresponding liquid mass content measured in our local coordinate system (the left-hand pane shows the data for water and the right-hand ethyl acetate).
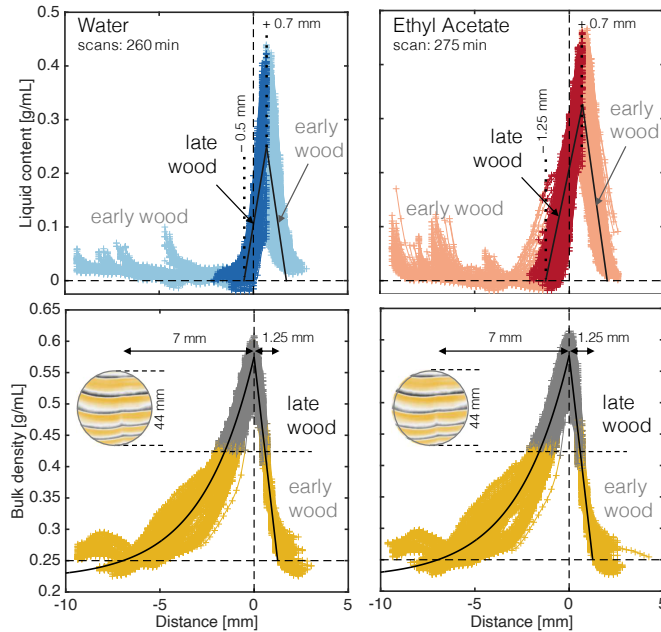
Fig. 8 Density variations in timber and associated distribution of liquid content following injection. The bottom plots represent bulk density profiles for each growth ring and for ~ 100 vertical transects (459 profiles in total) within the slice of the timber specimen located 100 mm from the injection port (shown in the inset of the plot, voxel dimensions: $(250 \times 250)\mu m^2$). For each profile, location "zero" is set as the point where the largest bulk density is measured and the separation between late (grey symbols) and early-wood (yellow symbols) is arbitrarily set at the mid-point between minimum and maximum densities, $\rho_b = 0.43\,g/cm^3$. The plot for water injection is on the left and for ethyl acetate is on the right. On the top plots, the same profiles are shown, but in terms of liquid content measured at 260 min (water) and 275 min (ethyl acetate) after start of injection. The darker and lighter symbols denote locations identified in the bulk density profiles as late and early-wood, respectively. Note that the late-wood density peak and the peak saturation levels are not aligned.

In both of the lower and upper panes of figure 8 the regions of relatively high density late-wood (with the threshold set to $0.43\,g/cm^3$, see [24]) are shown by darker colours. What is clear from the upper two panes is that these high density dark regions do not perfectly align with the peaks in liquid mass content for either fluid. More specifically, these peak liquid mass contents contribute about 45% (for ethyl acetate) and 31% (for water) of the total liquid content. In fact, it is evident that the peaks in density and the peaks in liquid

mass content are offset by approximately $+0.7\,\text{mm}$ (±0.25 mm), indicating that these efficient paths of liquid transport are evident both for the transport of water and for ethyl acetate. We note that the observed offset is not created by image resolution, because the two sets of scans (dry vs. water, as well as dry vs. ethyl acetate) have been reconstructed at the same image resolution. Notably, these paths lie just on the new growth side of the peak densities, i.e. they lie just outside the late-wood growth rings. Such a finding is novel and contrary to the assumptions made in other studies that the preferential pathways lie within the late-wood cells [11–13]. The conclusion that preferential transport occurs in the smaller late-wood cells led previous researchers [13] to logically surmise that capillary effects must be dominant and therefore that capillary effects give rise to the fastest transport. However, we showed that, even when driving pressures of just one atmosphere were applied, capillary effects accounted for less than 10% of the liquid transport [3]. Our findings resolve this apparent contradiction. By identifying that the efficient transport pathways occur away from local peaks in density we can conclude that capillary effects do not give rise to relatively fast transport under these modest driving pressures. Indeed from our CT measurements and the work of [24] we can imply that the pore space within the efficient transport paths are of intermediate size — see the data in Figures 7 and 8, which highlights that the peaks in the transport occur at locations where the density is low, i.e. within some of the largest early-wood cells. Therefore, the structure and number of bordered pits within the efficient transport paths must vary to some extent — we exploit this knowledge in our modelling (Section 4.1). It is worth noting that such a finding warrants reexamination of industrial approaches to the liquid treatment of timber. These may also encompass the energy intensive timber drying process, particularly those practices that exploit chemical treatment to minimise dimensional changes in wood and the associated damage [25]. As we have studied kiln-dried timbers, which have modified microstructures (e.g. aspirated pits) in comparison to greenwood, our work could also offer insights into the reversibility of the drying process.

4 Discussion

Timber is the only widely-used construction material we can grow [26], and architects and engineers are ever more demanding of its use [27]. Extending the use of wood in construction offers significant scope for mitigating the effect of CO_2 emissions on our climate [28]. Timber use can be increased by better modifying its mechanical properties or improving its resilience with liquids. At a laboratory scale, previous work that involves exposing the timber microstructure to aqueous chemical solutions which delignify the specimens prior to compression, demonstrates that timber can be processed into materials with unprecedented mechanical properties [29, 30]. In order to industrialise this process and exploit further natural benefits of timber, accurately predicting the transport of these liquids within timber is crucial. Here, we have examined the

liquid transport in kiln-dried, moderately-sized ($l = 200\,\mathrm{mm}$) timber specimens using a medical-grade CT scanner and identify previously unreported efficient transport paths within the timber. Identifying these pathways provides a step-change in our understanding of the transport of liquids within timber, which we expect to lead to significant improvements in industrial treatment processes.

We further discuss our findings below by presenting a model to describe liquid transport through the timber specimen by using a geometrical parameterisation of the pore space informed by high-resolution imaging. Furthermore, we reconcile our findings with those of previous radiographic studies of timber [11–13] by discussing results of experiments of spontaneous imbibition using both medical-grade CT scans and a high-precision micro-CT scanner.

4.1 Prediction of liquid transport in timber

Following [3], we utilise a model based on the Lucas-Washburn equation [16, 17] modified to reflect the statistical distribution of the timber pore space. We update the model [3] to reflect the experiments presented herein; namely, that the flow was forced, by imposing a constant driving pressure, to enter the timber specimens from one end and was free to leave (at atmospheric pressure) from the other. In so doing, the model predicts both the liquid uptake by the timber and the flow rate through the specimen — these predictions can be directly compared to estimates made from our experimental CT measurements and the injection pump logs, respectively. Moreover, whereas [3] looked to model pore space within early- and late-wood phase of wood (and the statistical variation within each), we herein look to examine the effect of efficient transport paths within the timber. As such, the spatially resolved time-lapse data presented in this study not only uncover details of the displacement process, but provide also a unique opportunity to inform the parameterisation of the model itself.

We parameterise the model using standard values for the fluid properties (see [31, 32] and Table 2). In our experiments we utilise timber specimens taken from the same batch of Sitka spruce as those examined by [24]. We base our geometrical parameterisation of the pore space on the values reported from their CT and micro-CT measurements [24]. Namely, we take the values: $L_T = 1.25 \pm 0.25\,\mathrm{mm}$ for the tracheid lengths (where the tolerances reflect the standard deviation); $r_T = 16 \pm 3\,\mu\mathrm{m}$ for the tracheid radii; and $\phi = 0.73$ for the porosity. The only remaining parameters, not recorded by their micro-CT measurements, remain the number of bordered pits per tracheid for which we take the values reported by [3] and the characteristic diameter thereof, $2a_p$ — which remains the only fitting parameter herein. From the data shown in Figure 8 we estimate that the efficient transport paths account for about 7% of the timber volume and we therefore take $\alpha = 0.93$ in the model.

Figure 9 presents the experimental data from our CT measurements and the injection pump logs, and compares these to model predictions. In order to fit the data, we take $2a_p = 0.078\,\mu\mathrm{m}$ for the characteristic diameter of the
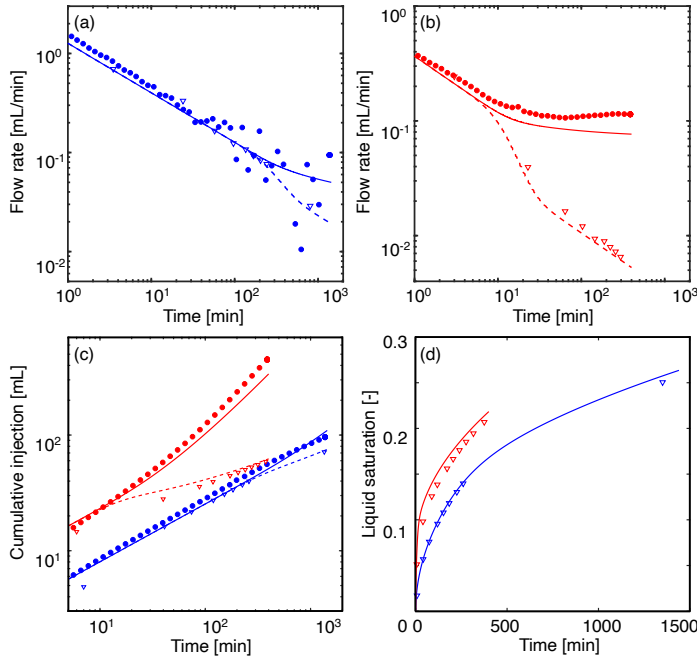
Fig. 9 Liquid injection and liquid uptake history for the experiments with water (blue) and ethyl acetate (red). In all plots, lines mark predictions from the model (§4.1), symbols mark experimental data; the latter include two sets of independent measurements, namely injection pump logs (filled circles) and X-ray CT (hollow triangles). (a) Injection and uptake rate for water; (b) Injection and uptake rate for ethyl acetate; (c) Cumulative injection and uptake; (d) Liquid uptake shown in terms of saturation.

bordered pits within the bulk of the specimen, for those within the efficient transport paths we take $2a_p = 0.14\,\mu$m for the experiments using water and $2a_p = 0.31\,\mu$m for the ethyl acetate experiments — all of which lie well within the range of measured values reported by [33]. Figure 9a and 9b show good agreement between the model predictions and the experimental data over a range of timescales from minutes right up to a day in the experiment using water. The model quantitatively captures the decreasing flow rate as the experiments evolve and correctly predicts the time at which liquid breaks through the specimen (reflected by the separation of the dashed and solid line for the model predictions, and the separation of the circular and triangular symbols for the experimental data). Furthermore, as the liquid break through signifies the time at which the efficient transport paths are (predominantly) saturated, thereafter the model predicts that the rate of uptake decreases dramatically (by a factor of approximately 3 for the water experiments and 10 for the ethyl acetate) — this dramatic decrease in uptake is precisely mirrored by the experimental data. Crucial to application, the total injected volume (Figure 9c) is predicted typically to an accuracy of within 20%, and the liquid saturation

(predictions of which would be vital to improve the industrial treatment of timber) is always accurately predicted to within 10% (Figure 9d). Moreover, the model enables us to examine the rate at which fluid advances along the efficient transport paths. We find that, on average, liquid advances along the efficient transport paths at rates between 10 and 30 times faster than in the bulk of the specimen. This highlights the significant role that these pathways must play in the transport within industrial sized pieces of timber.

Two comments are worth making with respect to the above analysis. First, our experiments used two fluids which are known to interact very differently with the cellular structure of timber (Section 2.1 and Table 2). It was necessary to characterise the bordered pits in the model differently for the two fluids, and this may indicate some effect of swelling on the flow passing through the pits — this remains a challenge for future research to investigate. Second, kiln drying causes aspiration of the bordered pits in most softwoods and its extent varies depending on the type and harshness of drying [34]. In our approach to the modelling, we have considered distinct values of the diameter of the bordered pits in the bulk of the specimen and in the efficient transport pathways. It follows that the flow behaviour observed in this study for both water and ethyl acetate may be the result of a characteristic spatial variability in the amount of aspiration following kiln drying. Future experiments where the same experimental protocol is applied to samples that have never been kiln-dried will provide more insight into this phenomenon.

4.2 Flow driven by spontaneous imbibition

Due to restrictions on the specimen size and the scan times we were unable to make reliable observations of the pressure driven transient flow via micro-CT. Thus, in order to validate our findings and compare to those of existing studies we carried out two additional sets of experiments in which the flow was driven solely by capillary action, herein spontaneous imbibition. These enabled measurements taken with a) a micro-CT scanner (resolution $(4\times4\times4)\mu m^3$ on specimens of length $7\,mm$) to be compared to those taken with b) our medical grade CT scanner (resolution $(0.25\times0.25\times1)mm^3$ on specimens of length $200\,mm$). The results of these experiments are shown in Figure 10 and Figure 11, respectively, enabling the visualisation and quantification of water uptake at different depths within the specimen (corresponding to different levels of liquid saturation). The results are illuminating, showing that, in agreement with previous studies of spontaneous imbibition [11–13], the dominant transport did occur in the smallest late-wood cells — as would be expected under capillary action. In fact, the 2D tomograms shown in Figure 10 provide direct evidence of significant accumulation of water just inside the late-wood growth rings; similarly, the profiles depicted in Figure 11 indicate that - when liquid uptake is significant (bottom plot) - the local maxima in the bulk density align by and large with those in the dry state. However, careful examination of the data of our CT scans, micro-CT data, and the images presented in

other studies, e.g. [11], show that there is also significant transport in certain of the largest early-wood cells — contrary to existing expectations, and, moreover, in agreement with the observations from our independent pressure driven flow experiments. We note that, whilst the terminal rise of the water will (for these experiments) be greatest in the smallest cells, identifying efficient transport paths in early-wood cells (for which the viscous retardation is least) provides sound reasoning as to why significant volumes of water rise more quickly through some of the largest early wood cells.
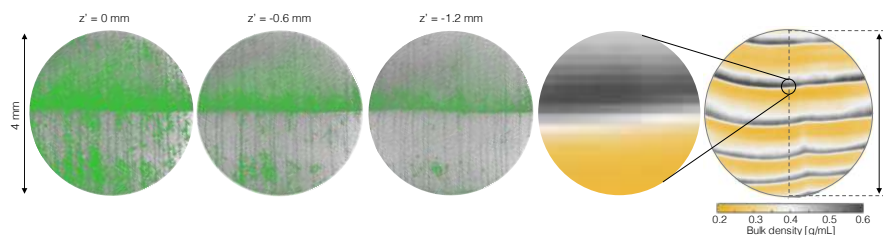
Fig. 10 2D tomograms acquired during a spontaneous imbibition experiment with water on the small 4 mm-diameter, 7 mm-long timber specimen. The first three tomograms on the left (voxel dimensions: $(4{\times}4)\mu\mathrm{m}^2$) refer to different depths within the specimen, from left (nearest the water source (0 mm, 0.6 mm and 1.2 mm), with the origin of the vertical coordinate set arbitrarily to the height of the first image). Water (highlighted in green) can be seen to have travelled farthest in the late-wood cells; crucially, significant transport can also be observed in a band of early-wood cells $\sim$1 mm from the early to late-wood transition. The last two tomograms on the right provide a comparison with images obtained on the medical CT scanner (voxel dimensions: $(250{\times}250)\mu\mathrm{m}^2$) on the large specimen (images are not registered).

5 Conclusions and implications

We have exploited medical grade CT imaging techniques with high-precision injection equipment to examine a widely used kiln-dried softwood timber in the presence of pressure driven flow. Knowledge of the timber micro-structure informs our analysis and enables the identification of efficient transport pathways within early-wood cells. We successfully model the flow within these pathways and within the bulk of the specimens and demonstrate that liquids are transported between 10 and 30 times faster along these efficient transport paths than within the bulk of the specimen. We validated these findings and successfully resolved the apparent inconsistency within the literature regarding the role of capillary effects and liquid transport in late-wood cells, by carrying out experiments of spontaneous imbibition, taking measurements using both our medical CT scanner and a micro-CT scanner.

The findings from our study are largely based on observations made on two specimens; this is undoubtedly a small number for a variable material, such as wood. Yet, a key aspect of our approach is the analysis of spatially resolved
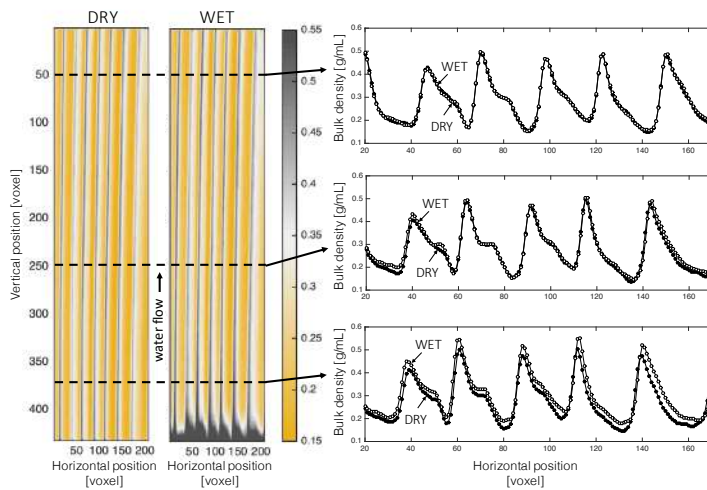
Fig. 11 2D vertical cross-section of the large timber specimen acquired prior to (image on the left) and during spontaneous water imbibition (image on the right, 70 hours after exposure to the water). The three plots on the right-hand side of the figure are bulk density profiles at three different depths (filled symbols refer to the dry specimen, while empty symbols refer to the wet specimen).

time-lapse fluid saturation data *within* the sample under study. To identify the efficient transport pathways, we have evaluated approx. 100 vertical transects across the wood specimen (resulting in approx. 500 density profiles and 20,000 saturation points) and we have done that for two independent experiments (water injection and ethyl acetate injection) – see Figure 8. We believe that this approach provides for a solid statistical basis in the evaluation of the fluid displacement process. In the approach to modelling, we have combined these data with a density-microstructure relationship derived for the same species of timber [24] and hypothesised that the first early-wood pits resist aspiration more strongly than the pits in the bulk of the specimen. That we are able to predict the macroscopic uptake and injection time-histories based on these physical measurements demonstrates that we have captured the specific physics of this process in our kiln-dried specimens.

Combining knowledge of these pathways with our predictive model we expect to be able to significantly improve the industrial treatment of timber, thereby enabling its mechanical properties and/or its resilience to be more effectively modified and better tailored to specific needs. Our findings therefore offer scope to extend the use of timber in construction - the only sustainable construction material that can be used at scale [26] - and so aid the positive changes that would be provided to our atmosphere and climate [28]. We propose that these techniques should be applied to hardwood timbers, green-wood timber, and be carried out also at the scale of micro-CT measurements. In so doing our findings offer genuine scope to increase the pallet of timber

products available to architects and engineers, and to better understand the energy intensive timber drying process.

Declarations

References

1. L.J. Gibson, J. Royal Soc. Interface **9**(76), 2749 (2012)
2. S. Malek, L.J. Gibson, Int. J. Solids Struct **113**, 118 (2017)
3. H.C. Burridge, G. Wu, T.P.S. Reynolds, D.U. Shah, R. Johnston, O.A. Scherman, M.H. Ramage, P.F. Linden, Sci. Rep. **9**(1), 20282 (2019)
4. A. Farina, I. Bargigia, E.R. Janeček, Z. Walsh, C. D'Andrea, A. Nevin, M. Ramage, O.A. Scherman, A. Pifferi, Opt. Lett. **39**(2), 228 (2014)
5. M.F. Rabbi, M.M. Islam, A.N.M.M. Rahman, Int. J. Eng. App. Sci. **2**(4), 75 (2015)
6. M.K. Dubey, S. Pang, S. Chauhan, J. Walker, Holzforschung **70**(8), 793 (2016)
7. Z. Walsh, E.R. Janeček, M. Jones, O.A. Scherman, Stud. Conserv. **62**(3), 173 (2017)
8. D.S. Belford, R.D. Preston, C.D. Cook, E.H. Nevard, Nature **180**(4595), 1081 (1957)
9. D.S. Belford, R.D. Preston, C.D. Cook, E.H. Nevard, J. App. Chem. **9**(3), 192 (1959)
10. D.S. Belford, J. App. Chem. **10**(8), 345 (1960)
11. M. Sedighi-Gilani, M. Griffa, D. Mannes, E. Lehmann, J. Carmeliet, D. Derome, Int. J. Heat Mass Tran. **55**(21-22), 6211 (2012)
12. M.A. Javed, P.M. Kekkonen, S. Ahola, V.V. Telkki, Holzforschung **69**(7), 899 (2015)
13. G. Desmarais, M.S. Gilani, P. Vontobel, J. Carmeliet, D. Derome, Transport Porous Med. **113**(2), 383 (2016)
14. W.B. Banks, Wood Sci. Technol. **15**(3), 171 (1981)
15. G. Bramhall, Wood Sci. Technol. **5**(2), 121 (1971)
16. R. Lucas, Colloid Polym. Sci. **23**(1), 15 (1918)
17. E.W. Washburn, Phys. Rev. **17**, 273 (1921)
18. G. Wu, D.U. Shah, E.R. Janeček, H.C. Burridge, T.P. Reynolds, P.H. Fleming, P.F. Linden, M.H. Ramage, O.A. Scherman, Wood Sci. Technol. **51**(6), 1277 (2017)
19. G.I. Mantanis, R.A. Young, R.M. Rowell, Holzforschung **48**(6), 480 (1994)
20. S.L. Wellington, H.J. Vinegar, Journal of Petroleum Technology **39**(08), 885 (1987)
21. C. Freyburger, F. Longuetaud, F. Mothe, T. Constant, J.M. Leban, Ann. For. Sci. **66**, 804 (2009)
22. H.J. Vinegar, S.L. Wellington, Review of Scientific Instruments **58**(1), 96 (1987)
23. J.M. Dinwoodie, Timber: Its nature and behaviour (Van Nostrand Reinhold Co. Ltd, 1981)

515   24. T.P.S. Reynolds, H.C. Burridge, R. Johnston, G. Wu, D.U. Shah, O.A. Scherman, P.F.
516   Linden, M.H. Ramage, J. Royal Soc. Interface **15**(142), 20180144 (2018)
517   25. S. Kumar, Wood and Fiber Sci. **26**(2), 270 (2007)
518   26. M.H. Ramage, H. Burridge, M. Busse-Wicher, G. Fereday, T. Reynolds, D.U. Shah,
519   G. Wu, L. Yu, P. Fleming, D. Densley-Tingley, J. Allwood, P. Dupree, P. Linden,
520   O. Scherman, Renew. Sustainable Energy Rev. **68**, 333 (2017)
521   27. W. Cornwall, Science **353**(6306), 1354 (2016)
522   28. J. Tollefson, Nature **545**, 280 (2017)
523   29. J. Song, C. Chen, S. Zhu, M. Zhu, J. Dai, U. Ray, Y. Li, Y. Kuang, Y. Li, N. Quispe,
524   Y. Yao, A. Gong, U.H. Leiste, H.A. Bruck, J.Y. Zhu, A. Vellore, H. Li, M.L. Minus,
525   Z. Jia, A. Martini, T. Li, L. Hu, Nature **554**(7691), 224 (2018)
526   30. M. Frey, D. Widner, J.S. Segmehl, K. Casdorff, T. Keplinger, I. Burgert, ACS Appl.
527   Mater. Interfaces **10**(5), 5030 (2018)
528   31. G.I. Mantanis, R.A. Young, Wood Sci. Technol. **31**(5), 339 (1997)
529   32. J.G. Speight, *et al.*, Lange's handbook of chemistry (McGraw-Hill New York, 2005)
530   33. J.F. Siau, Transport processes in wood (Springer-Verlag, 1984)
531   34. E.W.J. Phillips, Forestry **7**(2), 109 (1933)